

# Probing quantum corrected black hole through astrophysical tests with the orbit of S2 star and quasiperiodic oscillations

Tursunali Xamidov,<sup>1,\*</sup> Sanjar Shaymatov,<sup>1,2,3,4,†</sup> Bobomurat Ahmedov,<sup>1,5,6,‡</sup> and Tao Zhu<sup>2,7,§</sup>

<sup>1</sup>*Institute of Fundamental and Applied Research,*

*National Research University TIIAME, Kori Niyoziy 39, Tashkent 100000, Uzbekistan*

<sup>2</sup>*Institute for Theoretical Physics & Cosmology, Zhejiang University of Technology, Hangzhou 310023, China*

<sup>3</sup>*University of Tashkent for Applied Sciences, Str. Gavhar 1, Tashkent 100149, Uzbekistan*

<sup>4</sup>*Western Caspian University, Baku AZ1001, Azerbaijan*

<sup>5</sup>*Institute for Advanced Studies, New Uzbekistan University,*

*Movarounnahr str. 1, Tashkent 100000, Uzbekistan*

<sup>6</sup>*Institute of Theoretical Physics, National University of Uzbekistan, Tashkent 100174, Uzbekistan*

<sup>7</sup>*United Center for Gravitational Wave Physics (UCGWP),*

*Zhejiang University of Technology, Hangzhou 310023, China*

(Dated: March 11, 2025)

In this study, we explore the influence of the quantum correction parameter  $\xi$  on the motion of particles and the properties of quasiperiodic oscillations (QPOs) around a quantum-corrected black hole (QCBH). We first analyze the geodesics of a test particle and derive weak-field constraints on parameter  $\xi$  from the perihelion precession of orbits, using observations from the Solar System and the S2 star's orbit around SgrA\* supermassive black hole in the center of our galaxy. We obtain  $\xi \leq 0.01869$  and  $\xi \leq 0.73528$  using the analysis of Solar System observations and the orbit of the S2 star around SgrA\*, respectively. In the strong-field regime, we examine the dynamics of epicyclic motion around astrophysical black holes and, using observational data from four QPO sources and the Markov Chain Monte Carlo (MCMC) method, we determine the upper constraint  $\xi \leq 2.086$ . Our results provide new insights into the effects of quantum corrections on black hole spacetimes and highlight the potential of QPOs as a probe for testing quantum gravity in astrophysical environments.

## I. INTRODUCTION

Albert Einstein's theory of general relativity (GR) revolutionized our understanding of space and time by showing that gravity arises from the curvature of spacetime [1]. This framework provides a robust foundation for describing the macroscopic structure of black holes (BHs), successfully explaining phenomena such as the event horizon, gravitational waves (GWs) [2, 3], and the imaging of the supermassive black holes (SMBHs) at the center of the M87\* [4, 5] and SgrA\* [6, 7] galaxy. The direct detection of gravitational waves, along with the observation and analysis of the supermassive BH image through these instruments, provides explanations for astrophysical phenomena in a strong gravitational field regime. Furthermore, GR explains effects that Newtonian mechanics cannot, including the bending of light by massive objects, the perihelion precession of Mercury, and gravitational redshift. However, despite its success in explaining large-scale gravity, GR cannot describe the quantum nature of spacetime at microscopic scales. This limitation leaves fundamental questions unanswered. Although GR is a significant and main theory, it does not fully address unique singularity problems and quantum mechanical as-

pects of spacetime at microscopic scales [8]. Therefore, testing is required for the development of promising alternative theories that offer a fundamental understanding of these issues.

One of the main open problems is the existence of spacetime singularities [9, 10], which pose a fundamental challenge to classical general relativity. A promising way to address this issue involves modifying black hole solutions to include quantum effects. A particularly notable framework for such modifications is the Hamiltonian constraints approach [11, 12], which has played a significant role in the canonical quantization of general relativity. Using the Hamiltonian formulation, two black hole models were introduced in [13] to address an issue related to general covariance in spherically symmetric gravity, which arises when canonical quantum gravity is applied to develop a semiclassical black hole model. These two models differ in their choice of a quantum parameter.

It is important to explore whether the quantum parameters can leave any observational signatures for the current/or forthcoming observations, so the quantum effect on the black hole spacetime can be directly tested or constrained by observations. With this motivation, several observational or phenomenological implications of the quantum-corrected black hole spacetime have already been investigated [14–24]. In particular, the light ring and black hole shadow are useful for estimating black hole parameters, including mass, spin, the surrounding external field, and other physical properties. By analyzing the shadows of M87\* and SgrA\*, constraints on

\* xamidovtursunali@gmail.com

† sanjar@astrin.uz

‡ ahmedov@astrin.uz

§ zhut05@zjut.edu.cn

the quantum correction parameter  $\xi$  have been established [14, 15]. In addition, the quasinormal modes of the quantum corrected black hole have also been explored in [14, 16].

The detection of gravitational waves (GWs) and the imaging of the SMBHs at the centers of M87\* and SgrA\* are pivotal. Therefore, these observations are crucial not only for discovering new solutions in alternative theories of gravity but also for rigorously testing GR in the strong field regime and exploring various gravity theories through precise measurements of spacetime geometry parameters. High-frequency quasi-periodic oscillations (HF QPOs) in X-ray flux from BHs and neutron stars in X-ray binaries offer another promising avenue for testing gravity near BHs. Detected as narrow peaks in power density spectra, these QPOs originate within a few gravitational radii of the central object, depending solely on spacetime geometry and orbital radius. Analyzing QPOs in X-ray data from BH accretion disks [25] can thus reveal valuable insights into spacetime geometry within different gravity theories [26–28]. QPOs provide a powerful probe of astrophysical BH candidates in strong gravitational fields, offering valuable insights into the innermost regions of accretion disks and the masses, radii, and spin periods of white dwarfs, neutron stars, and BHs. Consequently, a deeper understanding of the rich nature of QPOs, particularly those described by X-ray power, is essential. This phenomenon has been regularly observed in microquasars, which are considered primary sources of low-mass binary systems (i.e., systems containing neutron stars or BHs). In this context, galactic microquasars are identified as sources of HF QPOs, characterized by upper ( $\omega_U$ ) and lower ( $\omega_L$ ) frequencies, often exhibiting a 3:2 ratio ( $\omega_U : \omega_L = 3 : 2$ ) [29–31]. HF QPO models have been extensively used to study epicyclic motions in BH accretion disks (see Refs. [32–34]). Notably, HF QPOs typically manifest as twin peaks, with pairs of frequencies observed in most cases. However, the mechanism underlying the occurrence of HF QPOs in specific regions of the accretion disk remains an open question, necessitating the development of explanatory models to address this issue [35]. Despite this uncertainty, alternative models have been proposed to explain such phenomena, including those incorporating magnetic fields around BHs [36–39]. In recent years, this topic has spurred significant research activity, with various authors exploring the analysis of HF QPOs within different resonance scenarios and frameworks [see, e.g., 40–59].

In this paper, we investigate the effect of the quantum correction parameter  $\xi$  on QPOs and the trajectory of particles moving around the QCBH. First, we derive the weak gravitational field constraints on the quantum correction parameter  $\xi$  within the observations of the Solar system tests and of the S2 star located in the star cluster close to the SgrA\* SMBH using the perihelion precession of particles orbiting the QCBH. Further, enhancing our understanding of the QPOs requires a detailed analysis of the epicyclic motion and the dynamics of timelike

particles in the close vicinity of the QCBH. Next, we apply the Markov Chain Monte Carlo (MCMC) method to determine the best-fit constraints on the parameter  $\xi$  in the strong gravitational field regime using observational data from four microquasars - GRO J1655-40, XTE J1550-564, GRS 1915+105, and H1743-322 - collectively referred to as QPO sources.

The paper is organized as follows: In Sec. II, we present the spacetime metric of the quantum-corrected black hole (QCBH) and analyze the geodesic motion of a test particle. We derive the weak-field constraints on the quantum correction parameter  $\xi$  by studying the perihelion precession of orbits in the Solar System and in the center of the Milky Way galaxy. In Sec. III, we investigate the dynamics of epicyclic motion and derive general expressions for the epicyclic frequencies. We further examine how the quantum correction parameter affects these frequencies. Finally, we use the Markov Chain Monte Carlo (MCMC) method in Sec. IV to determine strong-field constraints on parameter  $\xi$  using observational data from four QPO sources. We end with a conclusion in Sec. V.

## II. THE SPACETIME METRIC AND THE DYNAMICS OF MOTION

The spacetime metric describing a Quantum Corrected Black Hole (QCBH) is given by [13]

$$ds^2 = -f(r)dt^2 + f(r)^{-1}dr^2 + r^2(d\theta^2 + \sin^2\theta d\phi^2), \quad (1)$$

where

$$f(r) = \left(1 - \frac{2M}{r}\right) \left[1 + \frac{\xi^2}{r^2} \left(1 - \frac{2M}{r}\right)\right], \quad (2)$$

and  $M$  and  $\xi$  are the mass of the black hole and the quantum correction parameter, respectively. For further analysis, we shall for simplicity normalize the quantum correction parameter  $\xi \rightarrow \xi/M$ .

The Hamiltonian of a neutral particle moving around the QCBH is expressed as follows [60]

$$H = \frac{1}{2}g^{\alpha\beta}p_\alpha p_\beta, \quad (3)$$

where  $p^\alpha$  is the four-momentum of the neutral particle. In the spherical coordinate system,  $\alpha$  and  $\beta$  denote the indices of the  $(t, r, \theta, \phi)$  coordinates. The relationship between four-momentum and four-velocity is expressed by the equation  $p^\alpha = mu^\alpha$ , where  $m$  represents the mass of the neutral particle,  $u^\alpha = dx^\alpha/d\tau$  is the four-velocity. Furthermore,  $\tau$  defines the proper time. Since the spacetime metric (1) does not explicitly depend on the  $t$  and  $\phi$  coordinates, the following conserved quantities can be written [60]

$$\frac{p_t}{m} = g_{tt} \frac{dt}{d\tau} = -\mathcal{E}, \quad \frac{p_\phi}{m} = g_{\phi\phi} \frac{d\phi}{d\tau} = \mathcal{L}, \quad (4)$$

where  $\mathcal{E}$  and  $\mathcal{L}$  are the specific energy and the specific angular momentum of the particle. Knowing that the

Hamiltonian for a massive particle is  $H = -m^2/2$  and for a photon is  $H = 0$ , we can write the following equation using Eq. (4)

$$\frac{1}{2} (g^{rr} p_r^2 + g^{\theta\theta} p_\theta^2) + \frac{m^2}{2} (g^{tt} \mathcal{E}^2 + g^{\phi\phi} \mathcal{L}^2) = -\frac{m^2}{2}. \quad (5)$$

After defining  $\mathcal{H}$  as:

$$\mathcal{H} = \frac{1}{2} (g^{tt} \mathcal{E}^2 + g^{\phi\phi} \mathcal{L}^2 + 1), \quad (6)$$

and using

$$\begin{aligned} p_r &= g_{rr} p^r = g_{rr} m \frac{dr}{d\tau}, \\ p_\theta &= g_{\theta\theta} p^\theta = g_{\theta\theta} m \frac{d\theta}{d\tau}, \end{aligned}$$

we rewrite Eq. (5) as:

$$g_{rr} \left( \frac{dr}{d\tau} \right)^2 + g_{\theta\theta} \left( \frac{d\theta}{d\tau} \right)^2 = -2\mathcal{H}. \quad (7)$$

#### A. The geodesics of a test particle in the equatorial plane

We consider the motion of a particle confined to the equatorial plane, where  $\theta = \pi/2 = \text{const}$ . Under this assumption, the second term in Eq. (7) vanishes, and the equation simplifies to the following form:

$$g_{rr} \left( \frac{dr}{d\tau} \right)^2 = -2\mathcal{H}. \quad (8)$$

Using the conservation of angular momentum Eq. (4) and Eq. (8), we can derive the following equation of motion:

$$\left( \frac{dr}{d\phi} \right)^2 = -\frac{2g_{\phi\phi}^2 \mathcal{H}}{g_{rr} \mathcal{L}^2}. \quad (9)$$

Substituting Eq. (6) into Eq. (9) yields the following equation:

$$\left( \frac{dr}{d\phi} \right)^2 = \frac{r^4}{\mathcal{L}^2} \left( \mathcal{E}^2 - f(r) \left( 1 + \frac{\mathcal{L}^2}{r^2} \right) \right). \quad (10)$$

In the case of the particle moving in a circular orbit  $r = \text{const}$ , the first term of the same equation becomes zero, and the equation takes the following form

$$g_{\theta\theta} \left( \frac{d\theta}{d\tau} \right)^2 = -2\mathcal{H}. \quad (11)$$

The following conditions hold for the circular motion of a particle with the radius  $r = r_c$  in the plane  $\theta = \theta_c$ :

$$\mathcal{H}(r_c) = 0, \quad \partial_r \mathcal{H}|_{r_c} = 0, \quad (12)$$

and

$$\mathcal{H}(\theta_c) = 0, \quad \partial_\theta \mathcal{H}|_{\theta_c} = 0. \quad (13)$$

If we solve Eq. (6) using Eq. (4) along with conditions (12) and (13), we obtain the following expressions for the specific energy  $\mathcal{E}$  and specific angular momentum  $\mathcal{L}$

$$\mathcal{E} = -\frac{g_{tt}}{\sqrt{-g_{tt} - g_{\phi\phi} \Omega^2}}, \quad (14)$$

$$\mathcal{L} = \frac{g_{\phi\phi} \Omega}{\sqrt{-g_{tt} - g_{\phi\phi} \Omega^2}}, \quad (15)$$

where  $\Omega = d\phi/dt$  represents the angular velocity of the particle measured by distant observers. It can be calculated using the following expression [54, 61]:

$$\Omega = \frac{d\phi}{dt} = \pm \sqrt{-\frac{g_{tt,r}}{g_{\phi\phi,r}}}. \quad (16)$$

We can easily define  $\Omega$  from the metric (1) using the above expression as

$$\Omega = \pm \sqrt{\frac{Mr^3 - \xi^2 (8M^2 - 6Mr + r^2)}{r^6} \csc^2(\theta)}. \quad (17)$$

Thus, the following expressions for  $\mathcal{E}$  and  $\mathcal{L}$  can be written

$$\mathcal{E} = \frac{(2M - r) (2M\xi^2 - r(\xi^2 + r^2))}{r^2 \sqrt{(r - 3M) (2\xi^2(r - 2M) + r^3)}}, \quad (18)$$

$$\mathcal{L} = \sqrt{\frac{r^2 (Mr^3 - \xi^2 (8M^2 - 6Mr + r^2))}{(r - 3M) (2\xi^2(r - 2M) + r^3)}} \sin^2(\theta). \quad (19)$$

After making the following transformation

$$u = \frac{1}{r}, \quad \frac{du}{d\phi} = -\frac{1}{r^2} \frac{dr}{d\phi}, \quad (20)$$

Eq. (10) becomes:

$$\left( \frac{du}{d\phi} \right)^2 = \frac{\mathcal{E}^2}{\mathcal{L}^2} - \frac{f(u)}{\mathcal{L}^2} (1 + \mathcal{L}^2 u^2), \quad (21)$$

where

$$f(u) = (1 - 2Mu)(1 + \xi^2 u^2 (1 - 2Mu)). \quad (22)$$

By differentiating Eq. (21) with respect to  $\phi$ , we obtain the geodesic equation for a massive test particle moving around the quantum corrected black hole

$$\begin{aligned} \frac{d^2 u}{d\phi^2} &= \frac{M}{\mathcal{L}^2} - u + 3Mu^2 \\ -\xi^2 u(1 - 2Mu) &\left( \frac{1 - 4Mu}{\mathcal{L}^2} + 2u^2 - 6Mu^3 \right). \end{aligned} \quad (23)$$

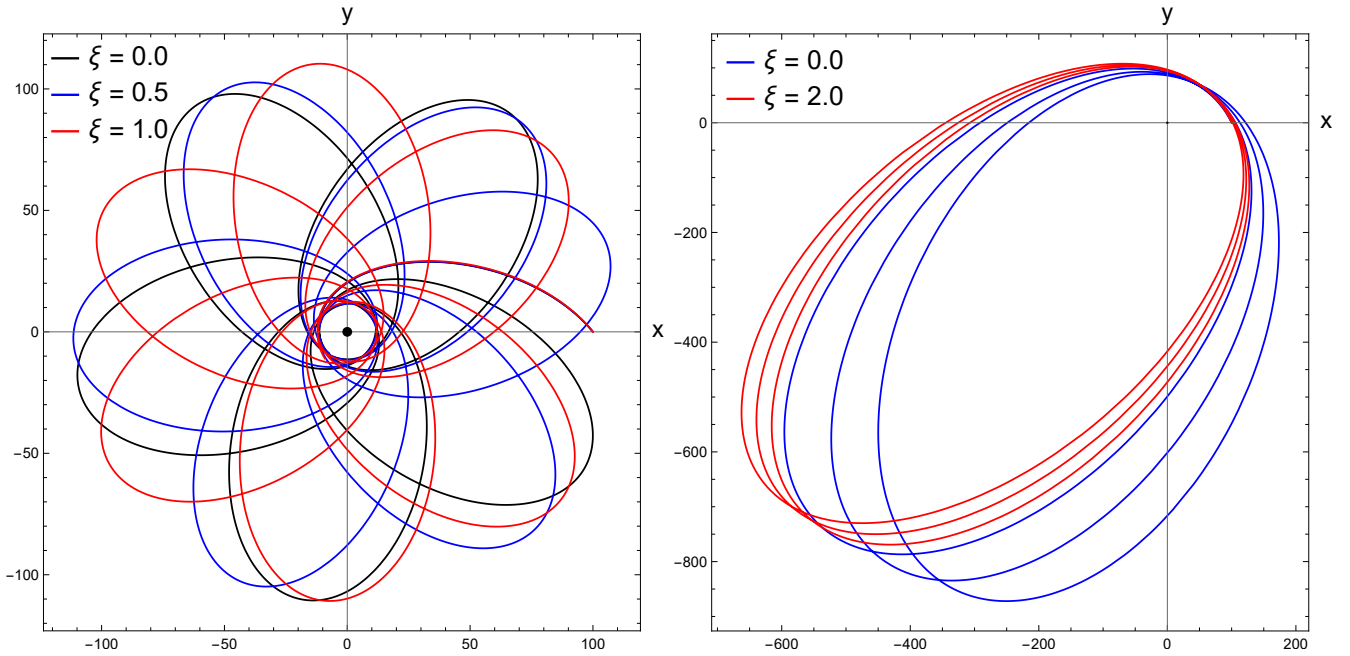


FIG. 1. The trajectories of a test particle moving in the equatorial plane ( $z = 0$ ) of a QCBH spacetime are shown for different values of the quantum correction parameter  $\xi$ . Left panel: The orbital motion of a particle with specific energy  $\mathcal{E} = 0.992$ , specific angular momentum  $\mathcal{L} = 5$ , and initial inverse radial coordinate  $u = 1/r = 0.01$  around a black hole of mass  $M = 1$ . Right panel: The effect of  $\xi$  on the perihelion shift of a particle with  $\mathcal{E} = 0.999$ ,  $\mathcal{L} = 12.5$ , and  $u = 1/r = 0.01$ . As  $\xi$  increases, the perihelion shift decreases, highlighting the impact of quantum corrections on the orbital dynamics.

## B. The perihelion shift

To determine the perihelion shift of the test particle's orbit, we rewrite Eq. (23)

$$\frac{d^2u}{d\phi^2} = \frac{M}{\mathcal{L}^2} - u + \frac{g(u)}{\mathcal{L}^2}, \quad (24)$$

where

$$\frac{g(u)}{\mathcal{L}^2} = 3Mu^2 - \xi^2 u(1 - 2Mu) \left( \frac{1 - 4Mu}{\mathcal{L}^2} + 2u^2 - 6Mu^3 \right).$$

Following the method presented in [62], we define the perihelion shift after a full revolution as:

$$\Delta\phi = \frac{\pi}{\mathcal{L}^2} \left| \frac{dg(u)}{du} \right|_{u=\frac{1}{b}}, \quad (25)$$

where  $b$  is defined as  $b = a(1 - e^2)$ . Here,  $a$  and  $e$  denote the semi-major axis and eccentricity of the orbit, respectively. Additionally, we define  $M$  as  $M \Rightarrow GM/c^2$ , and  $L^2$  as  $L^2 \Rightarrow GMa(1 - e^2)/c^2$  in SI units. After this transformation, the expression takes the following form:

$$\Delta\phi = \frac{6\pi GM}{ac^2(1 - e^2)} - \frac{\pi GM\xi^2}{ac^2(1 - e^2)} \left( 1 - \frac{6GM}{ac^2(1 - e^2)} - \frac{16G^2M^2}{a^2c^4(1 - e^2)^2} + \frac{60G^3M^3}{a^3c^6(1 - e^2)^3} \right). \quad (26)$$

For a numerical application, we consider the example of Mercury and use the following parameters

$$\begin{aligned} \frac{2GM_{\odot}}{c^2} &= 2.95325008 \times 10^3 \text{ [m]}, \\ a &= 5.7909175 \times 10^{10} \text{ [m]}, \\ e &= 0.20563069. \end{aligned}$$

With these parameters, we derive the following numerical result for Mercury's perihelion shift

$$\Delta\phi = 2\pi \times (7.98744 \times 10^{-8}) - 2\pi \times (1.33124 \times 10^{-8})\xi^2. \quad (27)$$

The first and second terms correspond to the prediction of general relativity and the influence of the quantum correction parameter, respectively. The measured perihelion shift of Mercury is expressed as [53, 63–65]

$$\Delta\phi_{\text{obs}} = 2\pi \times (7.98734 \pm 0.00037) \times 10^{-8} \text{ rad/rev}. \quad (28)$$

Using Eq. (27) and Eq. (28), we can estimate the possible value of the quantum correction parameter  $\xi$  for Mercury

$$\xi \leq 0.01869. \quad (29)$$

The influence of metric-affine geometry on particle motion becomes significant in strong gravitational regimes. One such scenario occurs in high-density astrophysical environments, such as near a supermassive black hole. High-precision astrometric observations near the compact source Sgr A\* and the S2 star, which orbits this

supermassive black hole and has an estimated mass between 10 and  $15M_\odot$ , allow us to estimate the quantum correction parameter  $\xi$  [66]. The S2 star can be treated as a test body moving along a geodesic trajectory. For this estimation, we adopt the following parameters

$$\begin{aligned} G &= 6.6743 \times 10^{-11} [\text{m}^3/(\text{kg} \cdot \text{s}^2)], \\ c &= 299,792,458 [\text{m/s}], \\ M_\odot &= 1.988416 \times 10^{30} [\text{kg}], \\ M_{\text{Sgr A}^*} &= 4.260 \times 10^6 M_\odot, \\ a_{\text{S2}} &= 970 [\text{au}], \\ 1 \text{ au} &= 1.495978707 \times 10^{11} [\text{m}], \\ e_{\text{S2}} &= 0.884649, \\ T_{\text{S2}} &= 16.052 [\text{years}]. \end{aligned}$$

Using these parameters, we obtain the following numerical result for the perihelion shift of the S2 star

$$\Delta\phi = 48.298 - 8.040 \xi^2 \left[ \text{''/year} \right]. \quad (30)$$

The observed perihelion shift of the S2 star orbiting Sgr A\* is given by

$$\Delta\phi = 48.298 f_{\text{SP}} \left[ \text{''/year} \right], \quad (31)$$

where  $f_{\text{SP}} = 1.10 \pm 0.19$  [66]. By utilizing Eqs. (30) and (31), we can determine the possible value of the quantum correction parameter  $\xi$  for the S2 star

$$\xi \leq 0.73528. \quad (32)$$

Fig. 1 illustrates the effect of the quantum correction parameter  $\xi$  on the trajectory of a particle orbiting a QCBH. The left panel of Fig. 1 illustrates the trajectory of a particle for different values of  $\xi$ , while keeping the initial conditions energy, angular momentum, and initial position constant. The black trajectory represents the classical motion of a particle orbiting a Schwarzschild black hole ( $\xi = 0.0$ ). As  $\xi$  increases, the trajectories deviate significantly from the classical case, demonstrating the impact of quantum corrections on the particles motion. The right panel of Fig. 1 depicts the effect of the quantum correction parameter on the perihelion shift of the particle. The graph shows that as  $\xi$  increases, the perihelion shift decreases. This trend is in agreement with the analytical result given by Eq. (26), confirming that quantum corrections reduce the relativistic precession of the orbit.

### III. THE DYNAMICS OF EPICYCLIC MOTION

Suppose that a particle is moving in a circular orbit of radius  $r = r_c$  in the equatorial plane  $\theta = \pi/2$ . If the particle deviates from its stable circular orbit by small perturbations  $\delta r$  and  $\delta\theta$ , it begins to oscillate around the circular orbit at  $r_c$ . These oscillations, characterized

by radial and latitudinal frequencies, are collectively referred to as epicyclic frequency. We can write the following expressions for  $r$  and  $\theta$  for this perturbations:

$$r = r_c + \delta r \quad \text{and} \quad \theta = \pi/2 + \delta\theta. \quad (33)$$

The change in  $\mathcal{H}$  due to this perturbation can be determined by expanding  $\mathcal{H}$  in a Taylor series about  $r = r_c$  and  $\theta = \pi/2$

$$\begin{aligned} \mathcal{H}(r, \theta) &= \mathcal{H}(r_c, \frac{\pi}{2}) + \delta r \partial_r \mathcal{H}(r, \theta) \Big|_{r_c, \frac{\pi}{2}} + \\ &+ \delta\theta \partial_\theta \mathcal{H}(r, \theta) \Big|_{r_c, \frac{\pi}{2}} + \delta r \delta\theta \partial_r \partial_\theta \mathcal{H}(r, \theta) \Big|_{r_c, \frac{\pi}{2}} + \\ &+ \frac{1}{2} \delta r^2 \partial_r^2 \mathcal{H}(r, \theta) \Big|_{r_c, \frac{\pi}{2}} + \frac{1}{2} \delta\theta^2 \partial_\theta^2 \mathcal{H}(r, \theta) \Big|_{r_c, \frac{\pi}{2}} + \\ &+ \mathcal{O}(\delta r^3, \delta\theta^3). \end{aligned} \quad (34)$$

According to conditions (12) and (13) for circular motion, the first four terms in the above expression vanish. Additionally, since they are very small, terms of  $\mathcal{O}(\delta r^3, \delta\theta^3)$  and higher can be neglected. As a result, the expression simplifies to the following form:

$$\mathcal{H}(r, \theta) = \frac{1}{2} \delta r^2 \partial_r^2 \mathcal{H}(r, \theta) \Big|_{r_c, \frac{\pi}{2}} + \frac{1}{2} \delta\theta^2 \partial_\theta^2 \mathcal{H}(r, \theta) \Big|_{r_c, \frac{\pi}{2}}. \quad (35)$$

Substituting expressions (33) and (35) into Eq. (7), we obtain the following equation:

$$\begin{aligned} g_{rr} \delta \dot{r}^2 + g_{\theta\theta} \delta \dot{\theta}^2 &= -\delta r^2 \partial_r^2 \mathcal{H}(r, \theta) \Big|_{r_c, \frac{\pi}{2}} - \\ &- \delta\theta^2 \partial_\theta^2 \mathcal{H}(r, \theta) \Big|_{r_c, \frac{\pi}{2}}. \end{aligned} \quad (36)$$

Here, since  $d$  and  $\delta$  commute, we have made the substitutions  $d\delta r/d\tau = \delta \dot{r}$  and  $d\delta\theta/d\tau = \delta \dot{\theta}$ . Taking the first derivative of both sides of the above equation with respect to proper time  $\tau$ , we obtain

$$\begin{aligned} \delta \dot{r} \left[ g_{rr} \delta \ddot{r} + \partial_r^2 \mathcal{H}(r, \theta) \Big|_{r_c, \frac{\pi}{2}} \delta r \right] + \\ + \delta \dot{\theta} \left[ g_{\theta\theta} \delta \ddot{\theta} + \partial_\theta^2 \mathcal{H}(r, \theta) \Big|_{r_c, \frac{\pi}{2}} \delta\theta \right] = 0. \end{aligned} \quad (37)$$

The solutions  $\delta \dot{r} = 0$  and  $\delta \dot{\theta} = 0$  are not satisfactory, as they indicate the absence of oscillations. In this case, the equation has a solution only if the expressions within the brackets are zero [38, 67]

$$\delta \ddot{r} + \Omega_r^2 \delta r = 0 \quad \text{and} \quad \delta \ddot{\theta} + \Omega_\theta^2 \delta\theta = 0, \quad (38)$$

where

$$\Omega_r^2 = \frac{\partial_r^2 \mathcal{H}(r, \theta) \Big|_{r_c, \frac{\pi}{2}}}{g_{rr}}, \quad (39)$$

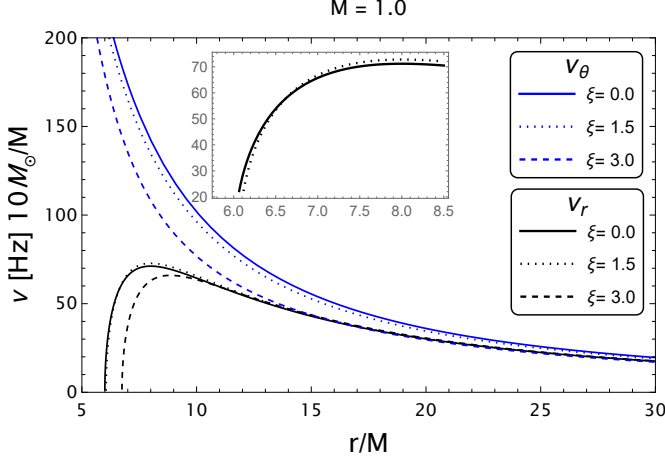


FIG. 2. The radial profile of the frequencies  $\nu_\theta$  and  $\nu_r$  measured by a distant observer is shown as a function of  $r/M$  for different values of the quantum correction parameter  $\xi$ .

$$\Omega_\theta^2 = \frac{\partial_\theta^2 \mathcal{H}(r, \theta)|_{r_c, \frac{\pi}{2}}}{g_{\theta\theta}}. \quad (40)$$

By substituting Eq. (18), (19) and (6) into Eq. (39) and (40), we obtain the following expressions for  $\Omega_r$  and  $\Omega_\theta$

$$\Omega_r^2 = \frac{3M\xi^2 r^3 (12M^2 - 8Mr + r^2) + Mr^6(r - 6M)}{r^6(r - 3M)(2\xi^2(r - 2M) + r^3)} - \frac{2\xi^4(r - 2M)^2(24M^2 - 13Mr + 2r^2)}{r^6(r - 3M)(2\xi^2(r - 2M) + r^3)}, \quad (41)$$

$$\Omega_\theta^2 = \frac{Mr^3 - \xi^2(8M^2 - 6Mr + r^2)}{r^2(r - 3M)(2\xi^2(r - 2M) + r^3)}. \quad (42)$$

Usually, it is not the local value of the epicyclic frequency that is important but the value measured by a distant observer, as many astronomical objects are located far away. The following equation gives the relationship between local and distant epicyclic frequencies:

$$\omega_{distant} = \frac{\Omega_{local}}{u^t}, \quad (43)$$

where  $u^t = dt/d\tau$ , which can be determined by substituting Eq. (14) into Eq. (4)

$$u^t = \frac{1}{\sqrt{-g_{tt} - g_{\phi\phi}\Omega^2}}. \quad (44)$$

Thus, the expression for the epicyclic frequencies measured by a distant observer is given as follows

$$\omega_r^2 = \frac{3M\xi^2 r^3 (12M^2 - 8Mr + r^2) + Mr^6(r - 6M)}{r^{10}} - \frac{2\xi^4(r - 2M)^2(24M^2 - 13Mr + 2r^2)}{r^{10}}, \quad (45)$$

$$\omega_\theta^2 = \frac{Mr^3 - \xi^2(8M^2 - 6Mr + r^2)}{r^6}. \quad (46)$$

To express the frequency in SI units (Hz), the following transformation is required

$$\nu_i = \frac{\omega_i}{2\pi} \frac{c^3}{GM}. \quad (47)$$

Fig. 2 presents the epicyclic frequencies  $\nu_r$  and  $\nu_\theta$  as a function of  $r/M$ , as measured by a distant observer, for different values of the quantum correction parameter  $\xi$ . Both  $\nu_r$  and  $\nu_\theta$  decrease as  $r/M$  increases. Higher values of the quantum correction parameter  $\xi$  result in lower oscillation frequencies, shifting  $\nu_\theta$  to the left and  $\nu_r$  to the right.

#### IV. CONSTRAINTS ON THE PARAMETERS OF THE QUANTUM CORRECTED BLACK HOLE THROUGH THE ASTROPHYSICAL QUASIPERIODIC OSCILLATIONS'S DATA

In this section, we analyze four distinct QPO sources from various X-ray binaries, using validated observational data, as presented in Table I to constrain the effects of the quantum correction parameter  $\xi$  in QCBH. We adopt the forced resonance model as the theoretical framework to constrain the quantum correction parameter  $\xi$  of QCBH [53, 68, 69]. Within this model, the upper ( $\nu_U$ ) and lower ( $\nu_L$ ) frequencies are defined as follows.

$$\nu_U = \nu_\theta + \nu_r, \quad \nu_L = \nu_\theta. \quad (48)$$

In Fig. 3, we plot the upper and lower frequencies of a particle near  $r_{\text{isco}}$  as a function of the black hole mass  $M$  for various values of  $\xi$ . The left panel of the figure illustrates the effect of  $\xi$  on the upper frequencies. Clearly, the upper frequency  $f_{\text{UP}}$  decreases as both  $\xi$  and  $M$  increase. As the mass  $M$  increases, the gravitational force that pulls the particle toward the black hole also becomes stronger. Consequently, the innermost stable circular orbit expands, causing the QPO to occur farther from the black hole. As a result, the QPO frequency decreases, as indicated by Eqs. (41) and (42). In the right panel of Fig. 3, the upper and lower frequencies of a particle near the innermost stable circular orbit  $r_{\text{isco}}$  are plotted as functions of  $M/M_\odot$  using the best-fit values of the quantum correction parameter  $\xi$ . The best-fit values of  $\xi$  for these QPO sources are  $\xi = 2.74 \pm 0.01$  for the upper frequency and  $\xi = 2.68 \pm 0.03$  for the lower frequency.

To estimate the limiting value of  $\xi$  for each QPO source, we used the *emcee* Python package [76], which employs the Markov Chain Monte Carlo (MCMC) method to constrain the physical parameters. The posterior probability distribution, based on Bayes' theorem, is expressed as:

$$P(\Theta|D, \mathcal{M}) = \frac{L(D|\Theta, \mathcal{M})\mathcal{P}(\Theta|\mathcal{M})}{P(D|\mathcal{M})}, \quad (49)$$

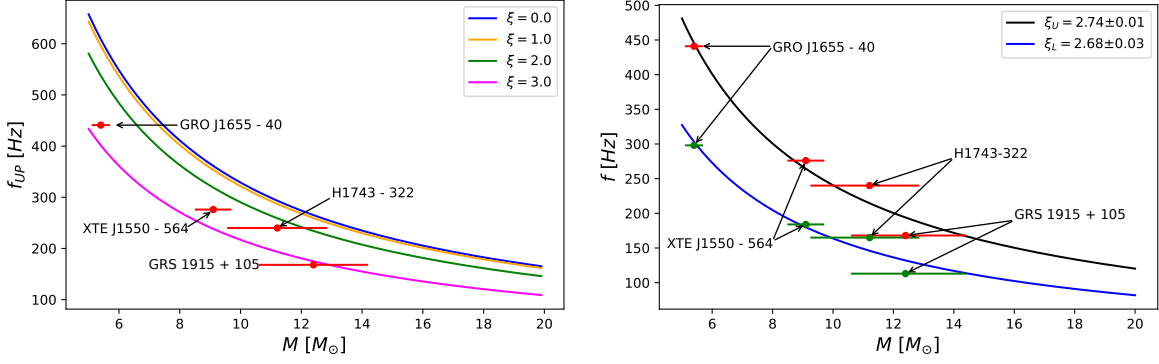


FIG. 3. Left: The upper  $\nu_U$  frequency is depicted as functions of the mass  $M$  for different values of the quantum correction parameter  $\xi$ , analyzed near the innermost stable circular orbit  $r_{\text{iscc}}$ . Red horizontal lines indicate the observational data for various QPO sources, with the width of these lines representing the uncertainty in the mass of the sources. Right: The upper and lower frequencies of a particle near the innermost stable circular orbit  $r_{\text{iscc}}$  are plotted as function of  $M/M_\odot$  for the best-fit values of the quantum correction parameter  $\xi$ . The black solid curve represents the best-fit curve of the upper frequency  $f_U$ , while the blue solid curve corresponds to the lower frequency  $f_L$ . Observational data for various QPO sources are shown as horizontal lines, where red lines indicate the upper frequency and green lines represent the lower frequency. The width of these horizontal lines reflects the uncertainty in the mass estimates of the sources.

	GRS 1915 + 105 [70]	H1743-322 [71, 72]	XTE J1550 - 564 [73, 74]	GRO J1655 - 40 [75]
$M[M_\odot]$	$12.4^{+2.0}_{-1.8}$	$11.21^{+1.65}_{-1.96}$	$9.1^{+0.61}_{-0.61}$	$5.4^{+0.3}_{-0.3}$
$\nu_U[\text{Hz}]$	$168^{+3.0}_{-3.0}$	$240^{+3.0}_{-3.0}$	$276^{+3.0}_{-3.0}$	$441^{+2.0}_{-2.0}$
$\nu_L[\text{Hz}]$	$113^{+5.0}_{-5.0}$	$165^{+9.0}_{-5.0}$	$184^{+5.0}_{-5.0}$	$298^{+4.0}_{-4.0}$

TABLE I. The mass, upper, and lower frequencies of the QPOs from the X-ray binaries selected for analysis.

Parameters	GRS 1915 + 105		H1743-322		XTE J1550 - 564		GRO J1655 - 40	
	$\mu$	$\sigma$	$\mu$	$\sigma$	$\mu$	$\sigma$	$\mu$	$\sigma$
$M/M_\odot$	12.4	0.6	11.21	0.6	9.1	0.6	5.4	0.3
$r/M$	7.4	0.3	7.26	0.3	7.2	0.3	7.3	0.3
$\xi/M$	Uniform [0, 5]		Uniform [0, 5]		Uniform [0, 5]		Uniform [0, 5]	

TABLE II. Gaussian priors for the selected X-ray binaries used in the MCMC analysis of QPOs occurring around QCBH.

where  $P(\Theta|D, \mathcal{M})$  represents the *posterior probability*,  $L(D|\Theta, \mathcal{M})$  is the *likelihood function*,  $\mathcal{P}(\Theta|\mathcal{M})$  is the *prior probability*, and  $P(D|\mathcal{M})$  serves as a *normalizing constant*. To specify the priors, we assume a Gaussian prior distribution for the model parameters within specified boundaries:

$$\mathcal{P}(\theta_i) \sim \exp \left[ \frac{1}{2} \left( \frac{\theta_i - \theta_{0,i}}{\sigma_i} \right)^2 \right], \quad \theta_{\text{low},i} < \theta_i < \theta_{\text{high},i}, \quad (50)$$

where  $\theta_i = [M, r, \xi]$  and  $\sigma_i$  are their corresponding standard deviations. The prior values for these parameters are adopted as presented in Table II.

For the quantum correction parameter  $\xi$ , we assume a uniform prior distribution over a specified range:

$$\mathcal{P}(\xi) = 1, \quad \text{for } \xi \in [0, 5], \quad (51)$$

otherwise, we set  $\mathcal{P}(\xi) = 0$ . This choice ensures that the parameter space remains constrained within a physically meaningful range.

Based on the upper and lower frequency expressions in Eqs. (48), our MCMC analysis incorporates data from both the upper and lower frequencies (see Table I). Consequently, the likelihood function  $L$  is expressed as:

$$\log L = \log L_U + \log L_L, \quad (52)$$

where  $\log L_U$  denotes the likelihood of the upper frequencies,

$$\log L_U = -\frac{1}{2} \sum_i \frac{(\nu_{U,obs}^i - \nu_{U,model}^i)^2}{(\sigma_{U,obs}^i)^2}, \quad (53)$$

and  $\log L_L$  represents the likelihood of the lower frequencies,

$$\log L_L = -\frac{1}{2} \sum_i \frac{(\nu_{L,obs}^i - \nu_{L,model}^i)^2}{(\sigma_{L,obs}^i)^2}. \quad (54)$$

Here,  $\nu_{U,obs}^i$  and  $\nu_{L,obs}^i$  represent the measured values of the upper and lower frequencies, while  $\nu_{U,model}^i$  and  $\nu_{L,model}^i$  correspond to their predicted values from the theoretical model. The terms  $\sigma_{U,obs}^i$  and  $\sigma_{L,obs}^i$  represent the statistical uncertainties associated with the measured upper and lower frequencies, respectively. Following the above setup, we perform an MCMC analysis to investigate the three-dimensional parameter space  $\{r, M, \xi\}$  associated with the quantum-corrected black hole (QCBH).

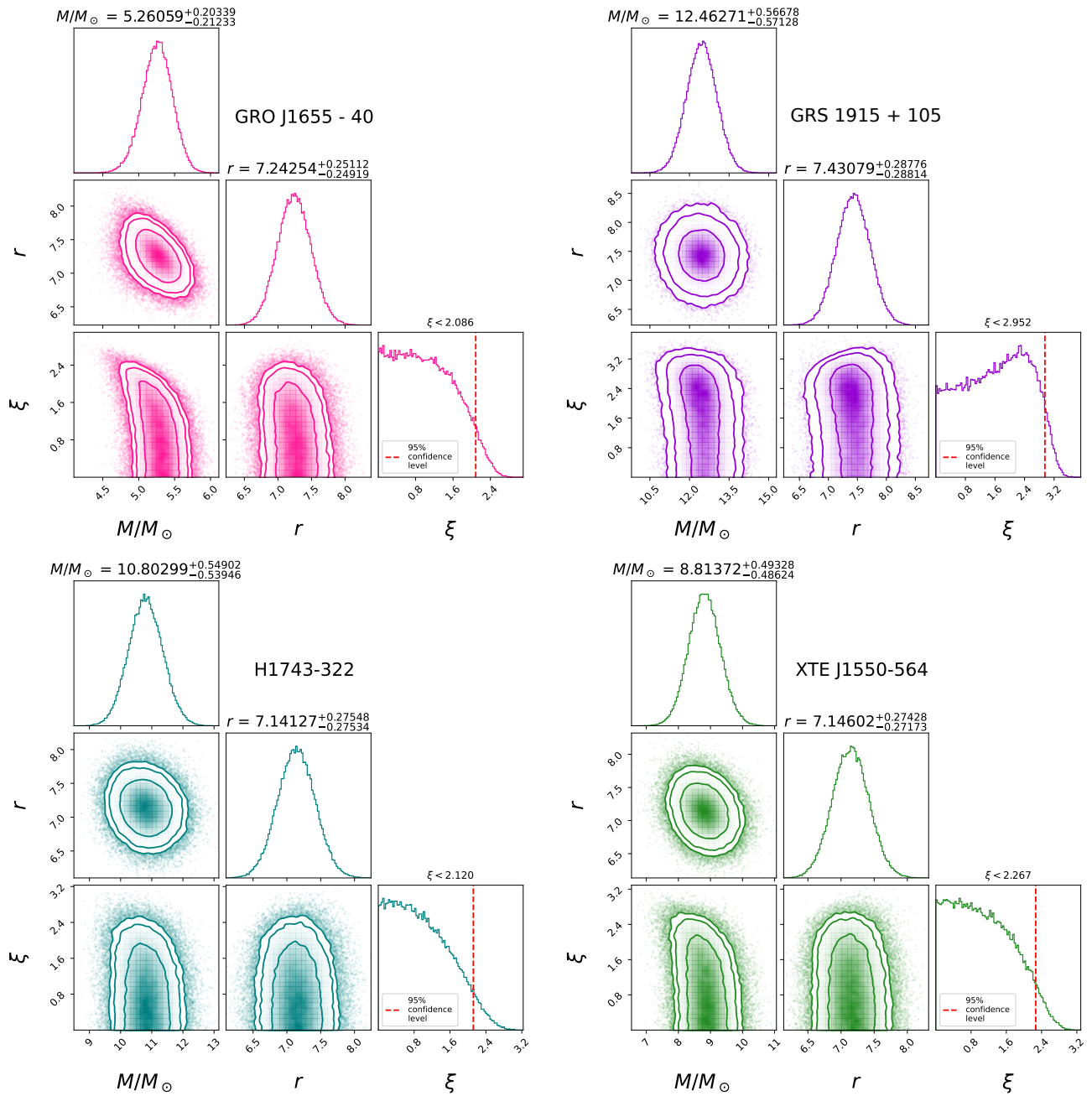


FIG. 4. Constraints on the parameters of QCBH from QPO observations of GRO J1655-40, GRS 1915+105, H1743-322, and XTE J1550-564 using the MCMC method. The plots show the posterior distributions for the black hole mass  $M$ , the dimensionless radius  $r/M$ , and the quantum correction parameter  $\xi$  within the forced resonance mode. The vertical dashed red lines indicate the 95% confidence level for  $\xi$ .

The best-fit values for these parameters are summarized in Table III, while Fig. 4 presents the MCMC posterior distributions for four selected astronomical objects. The shaded regions in the Fig. 4 correspond to the 68%, 90%, and 95% confidence levels, offering insight into the statistical uncertainties of the inferred parameters.

The results indicate that the best-fit value of the quantum correction parameter  $\xi$  is obtained from GRO J1655-

40, with an upper limit of  $\xi \leq 2.086$  at the 95% confidence level. GRO J1655-40 was selected due to its higher measurement accuracy compared to other QPO sources (see Table I). XTE J1550-564 and H1743-322 produced constraints close to that of GRO J1655-40, while GRS 1915+105 yielded a slightly higher upper limit. Therefore, we conclude that the quantum correction parameter

Parameters	GRS 1915 + 105	H1743-322	XTE J1550 - 564	GRO J1655 - 40
$M/M_{\odot}$	$12.45908^{+0.56642}_{-0.56419}$	$10.80299^{+0.54902}_{-0.53946}$	$8.81372^{+0.49328}_{-0.48624}$	$5.26059^{+0.20339}_{-0.21233}$
$r/M$	$7.43238^{+0.28877}_{-0.28595}$	$7.14127^{+0.27548}_{-0.27534}$	$7.14602^{+0.27428}_{-0.27173}$	$7.24254^{+0.25112}_{-0.24919}$
$\xi/M$	$< 2.952$	$< 2.120$	$< 2.267$	$< 2.086$

TABLE III. The best-fit values of QCBH parameters derived from QPOs in X-ray binaries.

is constrained to

$$\xi \leq 2.086 . \quad (55)$$

In this study, we obtained an upper limit of  $\xi \leq 2.086$ , which provides a tighter constraint compared to the limit  $\xi \leq 2.304$  obtained from the M87 black hole shadow [15] and the limit  $\xi \leq 2.866$  derived from the Sgr A\* shadow [14]. Unlike previous works that relied on black hole shadow observations to constrain  $\xi$ , our approach utilizes QPO data from X-ray binaries, offering an alternative and complementary method for testing quantum corrected black holes in strong gravitational regimes.

## V. CONCLUSIONS

In this work, we aimed to constrain the quantum correction parameter  $\xi$  for quantum corrected black holes (QCBHs) using QPO observations from X-ray binaries, along with the perihelion shifts of Mercury in the Solar System and the S2 star in SgrA\* SMBH environment. First, we analyzed the effect of the quantum correction parameter  $\xi$  on the motion of a particle moving in the equatorial plane around the QCBH. We derived an analytical expression for the perihelion shift in the case of elliptical motion. Our results indicate that the perihelion shift decreases as the parameter  $\xi$  increases (see Fig. 1). By calculating the perihelion shifts of Mercury and the S2 star and comparing the results with observational data, we evaluated the upper bounds of  $\xi$  to be  $\xi \leq 0.01869$  for Mercury and  $\xi \leq 0.73528$  for the S2 star.

Subsequently, we utilized QPOs to estimate the parameter  $\xi$  in strong gravitational field regime conditions. We derived expressions for the radial ( $\nu_r$ ) and latitudinal ( $\nu_{\theta}$ ) frequencies of a test particle in the QCBH spacetime. Our analysis showed that these frequencies decrease the parameter as  $\xi$  increases (see Figs. 2 and 3). Using the Markov Chain Monte Carlo (MCMC) method, we constrained the limiting values of the parameter  $\xi$  for four X-ray binaries. As a result, we obtained an upper limit of the parameter  $\xi \leq 2.086$ , providing tighter constraints compared to previous studies based on black hole shadows, such as those for M87 ( $\xi \leq 2.304$ ) and Sgr A\* ( $\xi \leq 2.866$ ) [14, 15].

These findings suggest that quantum gravitational effects are less significant in weak gravitational fields, where the parameter  $\xi$  is smaller. In contrast, the influence of the quantum correction parameter becomes more pronounced in strong gravitational fields, as evidenced by the larger upper bound of the parameter  $\xi$  obtained from QPO observations.

Our results provide new insights into the role of the quantum correction parameter in quantum corrected black holes. Future high-precision observations, particularly with next-generation telescopes, are expected to refine these constraints further, advancing our understanding of quantum gravitational phenomena.

## ACKNOWLEDGMENTS

The research is supported by the National Natural Science Foundation of China under Grant No. W2433018. Tao Zhu is also supported by the National Natural Science Foundation of China under Grants No. 12275238, the National Key Research and Development Program of China under Grant No. 2020YFC2201503, and the Zhejiang Provincial Natural Science Foundation of China under Grants No. LR21A050001 and No. LY20A050002.

- 
- [1] A. Einstein, *Annalen der Physik* **354**, 769 (1916).
  - [2] B. P. Abbott and et al. (Virgo and LIGO Scientific Collaborations), *Phys. Rev. Lett.* **116**, 061102 (2016), [arXiv:1602.03837 \[gr-qc\]](#).
  - [3] B. P. Abbott and et al. (Virgo and LIGO Scientific Collaborations), *Phys. Rev. Lett.* **116**, 241102 (2016), [arXiv:1602.03840 \[gr-qc\]](#).
  - [4] K. Akiyama and et al. (Event Horizon Telescope Collaboration), *Astrophys. J.* **875**, L1 (2019), [arXiv:1906.11238 \[astro-ph.GA\]](#).
  - [5] K. Akiyama and et al. (Event Horizon Telescope Collaboration), *Astrophys. J.* **875**, L6 (2019), [arXiv:1906.11243 \[astro-ph.GA\]](#).
  - [6] K. Akiyama and et al. (Event Horizon Telescope Collaboration), *Astrophys. J. Lett.* **930**, L12 (2022).
  - [7] K. Akiyama and et al. (Event Horizon Telescope Collaboration), *Astrophys. J. Lett.* **930**, L14 (2022).
  - [8] A. Ashtekar and E. Bianchi, *Rept. Prog. Phys.* **84**, 042001 (2021), [arXiv:2104.04394 \[gr-qc\]](#).
  - [9] R. Penrose, *Phys. Rev. Lett.* **14**, 57 (1965).
  - [10] S. W. Hawking and R. Penrose, *Proc R. Soc. Lond. A* **314**, 529 (1970).
  - [11] A. Ashtekar and J. Lewandowski, *Class. Quantum Gravity* **21**, R53 (2004), [arXiv:gr-qc/0404018 \[gr-qc\]](#).
  - [12] T. Thiemann, *Modern Canonical Quantum General Relativity* (2007).
  - [13] C. Zhang, J. Lewandowski, Y. Ma, and J. Yang, *arXiv e-prints*, [arXiv:2407.10168 \(2024\)](#), [arXiv:2407.10168 \[gr-qc\]](#).

- [14] R. A. Konoplya and O. S. Stashko, *arXiv e-prints*, [arXiv:2408.02578 \(2024\)](#), [arXiv:2408.02578 \[gr-qc\]](#).
- [15] Y.-H. Shu and J.-H. Huang, *arXiv e-prints*, [arXiv:2412.05670 \(2024\)](#), [arXiv:2412.05670 \[gr-qc\]](#).
- [16] M. Skvortsova, *arXiv e-prints*, [arXiv:2411.06007 \(2024\)](#), [arXiv:2411.06007 \[gr-qc\]](#).
- [17] W. Liu, D. Wu, and J. Wang, *Phys. Lett. B* **858**, 139052 (2024), [arXiv:2408.05569 \[gr-qc\]](#).
- [18] H. Liu, M.-Y. Lai, X.-Y. Pan, H. Huang, and D.-C. Zou, *Phys. Rev. D* **110**, 104039 (2024), [arXiv:2408.11603 \[gr-qc\]](#).
- [19] Y.-H. Shu and J.-H. Huang, (2024), [arXiv:2412.05670 \[gr-qc\]](#).
- [20] H. Jiang, M. Alloqulov, Q. Wu, S. Shaymatov, and T. Zhu, *Phys. Dark Universe* **46**, 101627 (2024).
- [21] Y. Du, Y. Liu, and X. Zhang, (2024), [arXiv:2411.13316 \[gr-qc\]](#).
- [22] Z. Ban, J. Chen, and J. Yang, (2024), [arXiv:2411.09374 \[gr-qc\]](#).
- [23] Y. Wang, A. Vachher, Q. Wu, T. Zhu, and S. G. Ghosh, (2024), [arXiv:2410.12382 \[astro-ph.CO\]](#).
- [24] U. Uktamov, M. Alloqulov, S. Shaymatov, T. Zhu, and B. Ahmedov, *Phys. Dark Universe* **47**, 101743 (2025), [arXiv:2412.01809 \[gr-qc\]](#).
- [25] M. A. Abramowicz and P. C. Fragile, *Living Rev. Relativ.* **16**, 1 (2013), [arXiv:1104.5499 \[astro-ph.HE\]](#).
- [26] C. Bambi, *Phys. Rev. D* **85**, 043002 (2012), [arXiv:1201.1638 \[gr-qc\]](#).
- [27] C. Bambi, J. Jiang, and J. F. Steiner, *Classical and Quantum Gravity* **33**, 064001 (2016), [arXiv:1511.07587 \[gr-qc\]](#).
- [28] A. Tripathi, J. Yan, Y. Yang, Y. Yan, M. Garnham, Y. Yao, S. Li, Z. Ding, A. B. Abdikamalov, D. Ayzenberg, C. Bambi, T. Dauser, J. A. Garcia, J. Jiang, and S. Nampalliwar, *arXiv e-prints* (2019), [arXiv:1901.03064 \[gr-qc\]](#).
- [29] W. Kluzniak and M. A. Abramowicz, *Acta Phys. Pol. B* **32**, 3605 (2001).
- [30] G. Török, M. A. Abramowicz, W. Kluzniak, and Z. Stuchlík, *Astron. Astrophys.* **436**, 1 (2005).
- [31] R. A. Remillard, J. E. McClintock, J. A. Orosz, and A. M. Levine, *Astrophys. J.* **637**, 1002 (2006), [arXiv:astro-ph/0407025 \[astro-ph\]](#).
- [32] Z. Stuchlík, A. Kotrlová, and G. Török, *Astron. Astrophys.* **552**, A10 (2013), [arXiv:1305.3552 \[astro-ph.HE\]](#).
- [33] L. Stella, M. Vietri, and S. M. Morsink, *Astrophys. J.* **524**, L63 (1999), [arXiv:astro-ph/9907346 \[astro-ph\]](#).
- [34] L. Rezzolla, S. Yoshida, T. J. Maccarone, and O. Zanotti, *Mon. Not. R. Astron. Soc.* **344**, L37 (2003), [arXiv:astro-ph/0307487](#).
- [35] G. Török, A. Kotrlová, E. Šrámková, and Z. Stuchlík, *Astron. Astrophys.* **531**, A59 (2011), [arXiv:1103.2438 \[astro-ph.HE\]](#).
- [36] A. Tursunov, Z. Stuchlík, M. Kološ, N. Dadhich, and B. Ahmedov, *Astrophys. J.* **895**, 14 (2020).
- [37] R. Pánis, M. Kološ, and Z. Stuchlík, *Eur. Phys. J. C* **79**, 479 (2019), [arXiv:1905.01186 \[gr-qc\]](#).
- [38] S. Shaymatov, J. Vrba, D. Malafarina, B. Ahmedov, and Z. Stuchlík, *Phys. Dark Universe* **30**, 100648 (2020), [arXiv:2005.12410 \[gr-qc\]](#).
- [39] S. Shaymatov, M. Jamil, K. Jusufi, and K. Bamba, *Eur. Phys. J. C* **82**, 636 (2022), [arXiv:2205.00270 \[gr-qc\]](#).
- [40] C. Germanà, *Phys. Rev. D* **98**, 083025 (2018), [arXiv:1810.12426 \[astro-ph.HE\]](#).
- [41] M. Tarnopolski and V. Marchenko, *Astrophys. J.* **911**, 20 (2021), [arXiv:2102.05330 \[astro-ph.HE\]](#).
- [42] V. I. Dokuchaev and Y. N. Eroshenko, *Phys. Usp.* **58**, 772 (2015), [arXiv:1512.02943 \[astro-ph.HE\]](#).
- [43] M. Kološ, Z. Stuchlík, and A. Tursunov, *Class. Quant. Grav.* **32**, 165009 (2015), [arXiv:1506.06799 \[gr-qc\]](#).
- [44] A. N. Aliev, G. D. Esmer, and P. Talazan, *Class. Quant. Grav.* **30**, 045010 (2013), [arXiv:1205.2838 \[gr-qc\]](#).
- [45] Z. Stuchlík, P. Slany, and G. Torok, *Astron. Astrophys.* **470**, 401 (2007), [arXiv:0704.1252 \[astro-ph\]](#).
- [46] Z. Stuchlík and J. Vrba, *Universe* **7**, 279 (2021), [arXiv:2108.09562 \[gr-qc\]](#).
- [47] L. Titarchuk and N. Shaposhnikov, *Astrophys. J.* **626**, 298 (2005), [arXiv:astro-ph/0503081](#).
- [48] M. Azreg-Aïnou, Z. Chen, B. Deng, M. Jamil, T. Zhu, Q. Wu, and Y.-K. Lim, *Phys. Rev. D* **102**, 044028 (2020), [arXiv:2004.02602 \[gr-qc\]](#).
- [49] K. Jusufi, M. Azreg-Aïnou, M. Jamil, S.-W. Wei, Q. Wu, and A. Wang, *Phys. Rev. D* **103**, 024013 (2021), [arXiv:2008.08450 \[gr-qc\]](#).
- [50] M. Ghasemi-Nodehi, M. Azreg-Aïnou, K. Jusufi, and M. Jamil, *Phys. Rev. D* **102**, 104032 (2020), [arXiv:2011.02276 \[gr-qc\]](#).
- [51] J. Rayimbaev, B. Majeed, M. Jamil, K. Jusufi, and A. Wang, *Phys. Dark Universe* **35**, 100930 (2022), [arXiv:2202.11509 \[gr-qc\]](#).
- [52] B. Narzilloev and B. Ahmedov, *Symmetry* **15**, 293 (2023).
- [53] S. Shaymatov, B. Ahmedov, M. De Laurentis, M. Jamil, Q. Wu, A. Wang, and M. Azreg-Aïnou, *Astrophys. J.* **959**, 6 (2023), [arXiv:2307.10804 \[gr-qc\]](#).
- [54] S. Shaymatov, K. Jusufi, M. Alloqulov, and B. Ahmedov, *Eur. Phys. J. Plus* **138**, 997 (2023), [arXiv:2303.06494 \[gr-qc\]](#).
- [55] G. Mustafa, G. D. Acan Yildiz, F. Javed, S. Maurya, E. Güdekli, and F. Atamurotov, *Phys. Dark Universe* **46**, 101647 (2024), [10.1016/j.dark.2024.101647](#).
- [56] T. Xamidov, U. Uktamov, S. Shaymatov, and B. Ahmedov, *Phys. Dark Universe* **47**, 101805 (2025).
- [57] C. Liu, H. Siew, T. Zhu, Q. Wu, Y. Sun, Y. Zhao, and H. Xu, *JCAP* **11**, 096 (2023), [arXiv:2305.12323 \[gr-qc\]](#).
- [58] M.-Y. Guo, M.-H. Wu, X.-M. Kuang, and H. Guo, *Eur. Phys. J. C* **85**, 95 (2025).
- [59] C. Liu, H. Siew, T. Zhu, Q. Wu, Y. Zhao, and H. Xu, (2023), [arXiv:2311.12423 \[astro-ph.HE\]](#).
- [60] C. W. Misner, K. S. Thorne, and J. A. Wheeler, *Gravitation* (W. H. Freeman, San Francisco, 1973).
- [61] S. Shaymatov, P. Sheoran, and S. Siwach, *Phys. Rev. D* **105**, 104059 (2022), [arXiv:2110.10610 \[gr-qc\]](#).
- [62] G. S. Adkins and J. McDonnell, *Phys. Rev. D* **75**, 082001 (2007), [arXiv:gr-qc/0702015 \[gr-qc\]](#).
- [63] S. Benczik, L. N. Chang, D. Minic, N. Okamura, S. Rayyan, and T. Takeuchi, *Phys. Rev. D* **66**, 026003 (2002), [arXiv:hep-th/0204049 \[hep-th\]](#).
- [64] L. Iorio, *Int. J. Mod. Phys. D* **24**, 1530015-343 (2015), [arXiv:1412.7673 \[gr-qc\]](#).
- [65] L. Iorio, *Astrophys. J.* **157**, 220 (2019), [arXiv:1810.13415 \[gr-qc\]](#).
- [66] GRAVITY Collaboration, *Astron. Astrophys.* **636**, L5 (2020), [arXiv:2004.07187 \[astro-ph.GA\]](#).
- [67] Z. Stuchlík and J. Vrba, *Eur. Phys. J. Plus* **136**, 1127 (2021), [arXiv:2110.10569 \[gr-qc\]](#).
- [68] E. Deligianni, B. Kleihaus, J. Kunz, P. Nedkova, and S. Yazadjiev, *Phys. Rev. D* **104**, 064043 (2021).

- [69] I. Banerjee, *Journal of Cosmology and Astroparticle Physics* **2022**, 034 (2022).
- [70] R. A. Remillard and J. E. McClintock, *Annu. Rev. Astron. Astrophys.* **44**, 49 (2006), [arXiv:astro-ph/0606352 \[astro-ph\]](#).
- [71] A. A. Molla, S. K. Chakrabarti, D. Debnath, and S. Mondal, *Astrophys. J.* **834**, 88 (2017), [arXiv:1611.01266 \[astro-ph.HE\]](#).
- [72] A. Ingram and S. Motta, *Mon. Not. R. Astron. Soc.* **444**, 2065 (2014), [arXiv:1408.0884 \[astro-ph.HE\]](#).
- [73] R. A. Remillard, M. P. Muno, J. E. McClintock, and J. A. Orosz, *Astrophys. J.* **580**, 1030 (2002), [arXiv:astro-ph/0202305 \[astro-ph\]](#).
- [74] J. A. Orosz, J. F. Steiner, J. E. McClintock, M. A. P. Torres, R. A. Remillard, C. D. Bailyn, and J. M. Miller, *Astrophys. J.* **730**, 75 (2011), [arXiv:1101.2499 \[astro-ph.SR\]](#).
- [75] S. E. Motta, T. M. Belloni, L. Stella, T. Muñoz-Darias, and R. Fender, *Mon. Not. R. Astron. Soc.* **437**, 2554 (2014), [arXiv:1309.3652 \[astro-ph.HE\]](#).
- [76] D. Foreman-Mackey, D. W. Hogg, D. Lang, and J. Goodman, *Publ. Astron. Soc. Pac.* **125**, 306 (2013), [arXiv:1202.3665 \[astro-ph.IM\]](#).